



A novel precast concrete beam-to-column connection with replaceable energy-dissipation connector: Experimental investigation and theoretical analysis

Chao Tong¹ · Jing Wu¹ · Chunyu Li²

Received: 7 February 2021 / Accepted: 1 June 2021 / Published online: 17 June 2021
© The Author(s), under exclusive licence to Springer Nature B.V. 2021

Abstract

To avoid the damage of the connection due to the overstrength of beam strength, and the alternation of the strength hierarchy in the structural system, a novel precast concrete beam-to-column connection is proposed herein. In the proposed connection, a novel replaceable energy-dissipation connector (REDC) was placed at the bottom of a hidden corbel. In addition, a narrow vertical slot was placed adjacent to the hidden corbel to reduce the beam overstrength. First, the structural features and mechanical mechanism of the proposed novel precast connection were discussed. Second, three low-cycle quasi-static loading tests were carried out on a single full-scaled specimen by using three REDCs of different sizes. The test results showed that the seismic performance of this novel precast connection was excellent and that the additional bending moment caused by beam overstrength in the novel precast connection was significantly lower than that of a conventional connection. Third, three finite element models were developed to further analyze how to reduce the additional bending moment and to always keep the top reinforcements in the elastic range. Finally, relevant design suggestions were provided. The additional bending moment of the novel precast connection designed according to the proposed formulas can be minimized. In view of this, the bending moments of the novel connection can be regarded as a controllable variable.

Keywords Precast concrete beam-to-column connection · Additional bending moment · Replaceable energy dissipation connector · Cyclic loading · Energy dissipation capacity · Seismic performance

Abbreviations

A_s	Equivalent cross-sectional area of the REDC core plate
A_s'	Area of the top reinforcement in beam
a	Whitney equivalent rectangular concrete stress block depth

✉ Jing Wu
seuwj@seu.edu.cn

¹ Key Laboratory On Concrete and Prestressed Concrete Structures of Ministry of Education, Southeast University, Nanjing 210096, China

² Key Laboratory of Roads and Railway Engineering Safety Control (Shijiazhuang Tiedao University), Ministry of Education, Shijiazhuang 050043, China

b	Section width of the beam
C_c <i>bottom</i>	Compression force provided by the bottom concrete compression zone
C_c <i>top</i>	Compression force provided by the top concrete compression zone
C_s	Compression force provided by the REDC
C_s'	Compression force provided by the top longitudinal reinforcements
c	Neutral-axis depth (measured from the top surface of the beam)
d	Beam effective depth
d'	Distance between the extreme top fiber and the centroid of top longitudinal reinforcement
d_c	Depth of the concrete top-hinge in this novel precast connection
d_{rein}	Diameter of the top longitudinal reinforcement
E_c	Elastic modulus of the concrete
E_s	Elastic modulus of the steel
e	Flow potential eccentricity of the concrete
F_{max1}	Maximum positive force
F_{max2}	Maximum negative force
f_{bf}/f_{c0}	Ratio of the concrete compressive strength under biaxial loading to uniaxial compressive strength
f_c'	Specified 28-d concrete compressive strength
f_{co}'	Unconfined concrete compressive strength
f_{co}'	Confined concrete compressive strength
f_l'	Effective lateral confining stress on the concrete
f_y	Yield strength of the REDC core plate
f_y'	Yield strength of the top reinforcement
h_0	Effective height of the cross section (h_0 represents the d_c in this novel precast connection)
K	Ratio of the of the second stress invariant on the tensile meridian to that on the compressive meridian
M_{add}	Additional bending moment
$M_{addnovel}$	Additional bending moment of novel beam-column connection proposed in this paper
M^{+}_{cmax}	Maximum controllable positive bending moment
M^{-}_{cmax}	Maximum controllable negative bending moment
$M^{+}_{c,y}$	Controllable positive yield bending moment
$M^{-}_{c,y}$	Controllable negative yield bending moment
M^{+}_{max}	Maximum positive bending moment of the specimen in Test 1
M^{-}_{max}	Maximum negative bending moment of the specimen in Test 1
M^{+}_n	Positive bending moment of the novel beam-to-column connection
M^{-}_n	Negative bending moment of the novel beam-to-column connection
n_{f1}	Number of cycles at θ_{f1} , level
n_{f2}	Number of cycles at θ_{f2} , level
T_s	Tension force provided by the REDC
V^{+}	Positive shear force
V^{-}	Negative shear force
V_{s^c}	, Shear force transferred through the compression concrete zone
V_{s^c} <i>corbel</i>	, Shear capacity provided by the hidden corbel
ν_c	Poisson's ratio of the concrete
α_1	Concrete stress block factor
β	Concrete stress block factor

β_c	Coefficient of concrete strength (=1.0 for C50 concrete)
γ	Strain-hardening coefficient of the REDC
δ_1	Buckling amplitude of the REDC core plate in Test 1
δ_2	Buckling amplitude of the REDC core plate in Tests 1 and 2
η	Reduction factor of the hardening modulus when model at the elastoplastic stage
$\theta_{j1,level}$	Drift level in the loading protocol corresponding to the first fractured side of the REDC core plate
$\theta_{j2,level}$	Drift level in the loading protocol corresponding to the second fractured side of the REDC core plate
θ_{max1}	Maximum positive drift
θ_{max2}	Maximum negative drift
ϕ	Amplification coefficient of the confined concrete compressive strength
ψ	Dilation angle of the concrete

1 Introduction

In recent years, precast concrete structures have been comprehensively developed and have gradually replaced traditional cast-in-place structures. This has promoted the process of construction industrialization and satisfied the needs of the future development of the construction industry (Hassoun and Al-Manaseer 2020). Although these “wet” fabricated structures can be equivalent to or close to cast-in-place structures, they inherit the damage dispersion of the cast-in-place structures under strong earthquakes (Liu et al. 2017). The precast concrete systems were designed and detailed such that their behavior under earthquakes was similar to the behavior of monolithic cast-in-place reinforced-concrete (RC) structures. This precast construction technique is often referred to as “wet” joint construction (Rodgers et al. 2012; Au 2010; Muir 2014). Under seismic action, the ductility of the plastic hinge at the beam end of the structures mainly depends on the yield of the longitudinal reinforcements at the beam end. Because of the crushing of the concrete in the compression zone and the buckling of the longitudinal reinforcements caused by the rotation of the plastic hinge, the moment capacity decreases rapidly. This type of failure occurs particularly readily under a negative moment due to the larger thickness of the compression zone at the bottom of the beam. After an earthquake, although the cracked or slightly crushed concrete can be repaired, the buckled or yielded longitudinal reinforcements are difficult to repair or replace. Therefore, it is difficult to repair the cast-in-place structures and most of the “wet” precast structures after an earthquake. Numerous seismic damage investigations revealed the phenomenon of “strong beam and weak column” in structures under earthquake excitation, although the seismic principle of “strong column weak beam” was universally emphasized in the design philosophy. A significant increase in the beam overstrength moments and hence the column moment demands might alter the strength hierarchy such that undesirable column hinging might occur and, in the worst case, could result in undesirable soft-story failure (Huang et al. 2020a, b). This is mainly attributed to the large area of the slab reinforcements in the flange of the frame beam, which contributes to the bending moment resistance together with the longitudinal reinforcements in the beam under a negative bending moment, resulting in an overstrength bending moment of the beam. Thus, the ideal hinge mechanism cannot be realized. This significant problem in

prefabricated concrete structures, particularly in “wet” prefabricated concrete structures, must be addressed.

In recent decades, the seismic performance of fabricated structures has been studied thoroughly and comprehensively. In the 1970s, Blakeley and Park (1971), and Thompson (1975) experimentally investigated the joints and structures of prefabricated frames to understand their behavior under cyclic load reversals. The test results indicated that prefabricated concrete structures had favorable integrity, ductility properties, and deformation recovery capabilities. The Precast Seismic Structural System Research Program (PRESSS) began in 1991 and was jointly undertaken by researchers in the United States and Japan. As one of the first research projects in this field, the PRESSS involved a detailed investigation of precast concrete structures (Priestley 1991, 1996; Priestley and Macrae 1996; Vasconez et al. 1998). In 2003, the European Union initiated a seismic research project for precast concrete structures based on Eurocode 8 (Fan et al. 2007), in which the seismic performance of beam-to-column connections and frames was investigated, and useful results were obtained. Nakaki et al. (1994) proposed precast concrete beam-to-column connections with a Dywidag ductile connector (DDC). Englekirk (1995) tested precast concrete beam–column connections with DDCs under quasi-static cyclic loading to evaluate their seismic performance. Under 3.5% interstory drift, the connections and components exhibited no obvious damage. Englekirk (1996) first used a DDC in the Wiltern Center Parking in Los Angeles. This structure has been analyzed by Englekirk (2002) and applied to famous buildings, including the Highland Center in Hollywood and the Paramount apartments in San Francisco. Chang et al. (2012, 2014) tested full-scale and scaled specimens of frames with DDCs. The results confirmed that the connections with DDCs had a stable energy dissipation capacity and that the seismic performance of the DDC frames was better than that of conventional frames. Kenyon (2008) conducted a finite element simulation to evaluate the seismic performance of precast concrete frames with DDCs.

Additionally, according to the damage avoidance design (DAD) approach (Bacht et al. 2011; Mander and Cheng 1997; Mander et al. 2009; Huang et al. 2020a, b), various yielding steel devices have been proposed and used in structures. Damage avoidance could be achieved in moment frames by using special devices whose dissipative performance does not degrade with use. Different from the conventional moment frames, most precast frames were designed according to the DAD approach. This principle reduced the amount of frame repair needed, and the minimization of disruptions substantially reduced the economic and business impacts. Amaris et al. (2008) and Marriott (2009) proposed a tension and compression yield energy-dissipation device. However, this type of energy-dissipation device was installed outside the beams. Thus, the transfer force was indirect and easily resulted in the failure of the anchoring of the conversion block. Golondrino et al. (2018, 2019) tested and simulated an asymmetric friction energy-dissipation device and applied it to steel structures. Rodgers (2009) tested a series of lead squeeze dampers. Oh et al. (2009) and Köken and Köroğlu (2013) tested full-scale specimens of steel beam–column connections with steel slit dampers and compared them with conventional steel connections. The test results indicated that the steel slit damper provides a reliable energy-dissipation capacity. Chi et al. (2012) experimentally and analytically investigated the cyclic response of a posttensioned column base connection with a buckling-restrained steel (BRS) plate. The results indicated that the BRS plate had good energy-dissipation capacity when yielding under tension and compression. These steel energy-dissipation devices have an excellent and stable energy-dissipation capacities but have disadvantages; e.g., they have a complex structure, require extra space, and are difficult to replace.

Another consequence of plastic hinge formation is beam elongation. Over the course of a significant seismic event, a plastic hinge can lengthen by 2–5% of the beam depth (Fenwick et al. 1995). On the one hand, beam elongation increases the flexural capacity, leading to the phenomenon of a “strong beam and weak column”. On the other hand, beam elongation can increase the lateral resistance of a moment resisting frame and cause significant damage to the floor diaphragm (Bull 2003; Peng et al. 2009). To solve this problem, Ohkubo et al. (2009) proposed a slotted beam-to-column connection and performed experiments to examine the shear transfer mechanism in the beam-end region. The results indicated that the slotted beams had good flexural characteristics. Ohkubo and Hamamoto (2004) tested an RC slotted-beam structure with a floor slab to investigate the damage to the floor slab. The results indicated that the cracks and damage in the floor slab for slotted-beam frames were significantly lower than those for the conventional frames. Au (2010), Byrne and Bull (2012), and Muir et al. (2013) tested slotted-beam connections and frames and verified that the slotted-beam structures had good seismic performance. Additionally, Oudah and El-Hacha (2017) tested numerous specimens of slotted-beam connections to examine the effects of the vertical slot position on the seismic performance and damage to the connection. At present, research on slotted-beam connections mainly focuses on cast-in-place concrete frame structures, and there is little research on fabricated frame structures.

To address the aforementioned issues, a novel precast beam-to-column concrete connection with a replaceable energy-dissipation connector (REDC) is proposed herein. An REDC was connected to the longitudinal reinforcements in the beam and column by connecting blocks and horizontally aligned with the longitudinal reinforcement at the bottom of the connection. A hidden corbel was used to provide a sufficient vertical shear capacity and to facilitate construction of the beam and column assembly. A vertical slot was installed in the bottom of the beam and adjacent to the hidden corbel to reduce the thickness of the compression zone. The inclusion of the vertical slot allowed seismic rotations to occur around the remaining concrete top hinge such that deformations were accommodated by opening and closing of the gap. When the yield-capacity ratio of the top reinforcements to the bottom REDC was increased and the thickness of the concrete compression zone was reduced, the neutral axis of the connection moved upward, and the additional bending moment caused by the beam overstrength of the novel precast connection was reduced. In addition, when the frame composed of these novel connections was subjected to earthquake ground motions, the damage to the structure was mainly concentrated in the REDCs. After an earthquake, the structure can be repaired quickly by replacing the REDCs. Because of the reduction in the additional bending moment, the moment capacity of the connection was governed by the REDCs as much as possible, and the principle of “strong column weak beam” was easily realized. Therefore, the principles of “strong shear weak moment” and “strong connection weak member” could be achieved. In this study, the seismic performance of the novel precast connection was investigated via theoretical analysis, experimental research, and numerical analysis. Finally, relevant design suggestions for reducing the additional bending moment were proposed based on the numerical analysis results.

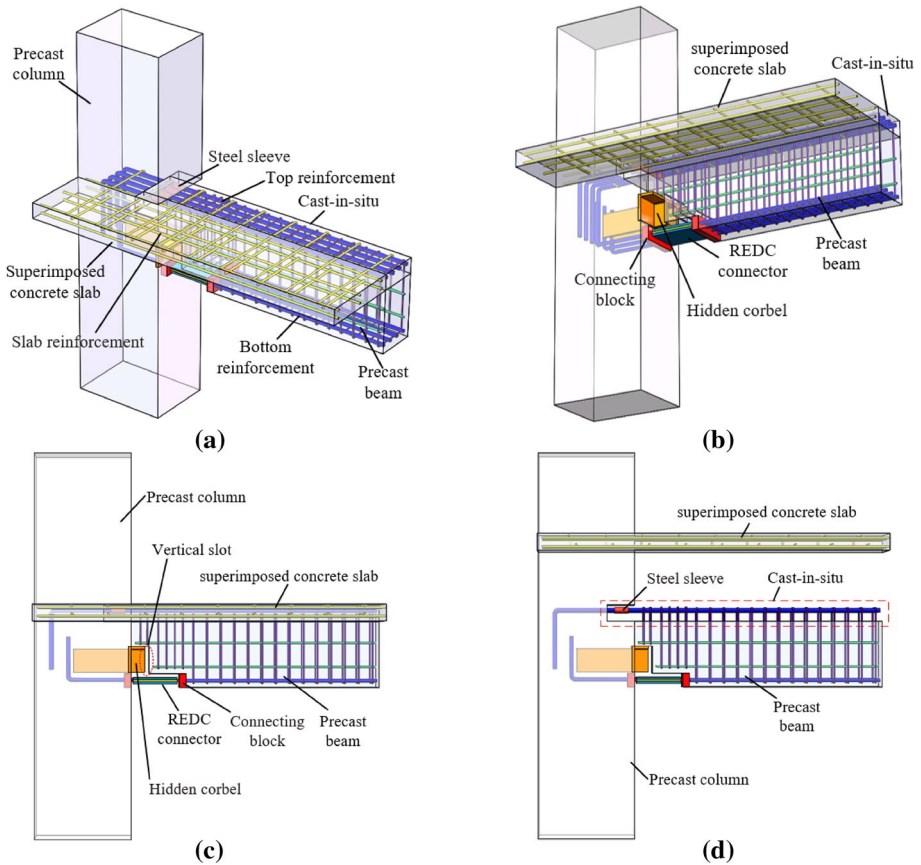


Fig. 1 Description of the novel precast concrete beam-to-column connections with the REDC: **a** side elevation (from top), **b** side elevation (from bottom), **c** front elevation, and **d** exploded view

2 Novel precast concrete beam-to-column connection with REDCs

2.1 Connection overview

A schematic configuration of the novel precast connection assembly is presented in Fig. 1. The connection was composed of four main parts: a precast concrete beam, a precast concrete column, an REDC, and a hidden corbel. As shown in Fig. 1a, the top longitudinal reinforcements in the connection were connected by steel sleeves. The yield capacity of the top longitudinal reinforcements (containing slab reinforcements) exceeded the yield capacity of the REDC core plate. As shown in Fig. 1b, the hidden corbel was embedded in the column and lapped with the rabbet of the precast beam. The π -shaped hidden corbel consisted of two welded steel plates; these plates contributed to the shear and bending capacities of the hidden corbel. An REDC was connected to the longitudinal reinforcements in the beam and column by connecting blocks and horizontally aligned with the longitudinal reinforcement at the bottom of the connection. Note that the two connecting blocks were embedded in the beam and column. In addition,

carbon dioxide gas shielded arc welding was used to weld the core plate and the connecting blocks, and the type of welding wire used was ER50-6. As shown in Fig. 1c, a vertical slot was installed at the bottom of the beam, immediately adjacent to the hidden corbel. Figure 1d shows an exploded view of the connection formed by moving the superimposed concrete slab upward. In Fig. 1d, the red rectangle (dashed line) is the cast-in-situ part of the beam and column.

Compared with the conventional beam-to-column connection, the advantages of the novel connection can be summarized as follows: First, the novel connection can avoid the damage of the joint area and column due to beam overstrength, and the alternation of the strength hierarchy in the structural system. In other words, it is more convenient to realize the seismic principle of “strong column weak beam” with this connection. It is well known that a beam overstrength results in obvious damage to the joint area and the column. Reducing the additional bending moment can effectively control the beam overstrength to prevent damage to the connection. The additional bending moment of the novel precast concrete beam-to-column connection designed according to the formulas proposed in this paper can be reduced as much as possible. Second, the novel beam-to-column connection can effectively realize the DAD approach because the damage of the novel connection is mainly concentrated in the REDC core plate. After an earthquake, these structures can be repaired quickly by replacing the REDCs. Last, the novel precast connection flexural response (controllable bending moment) is beneficial in the engineering design of the structures formed by this novel connection. The bending moments of the novel connection can be regarded as a controllable variable because of the reduction in the additional bending moment of the novel precast concrete beam-to-column connection. The bending moments of the novel connection are governed by the yielding of the REDC core plate. Therefore, this characteristic makes the engineering design of structures formed by this novel connection more convenient.

2.2 Details of the REDC

The REDC was a buckling-restrained energy dissipater proposed by Xie (2020). In addition, Li et al. (2020) proposed and tested a precast concrete frame with REDCs (REDC-PCF). Figure 2a–d show the details and testing of the REDC. The REDC was assembled with bolts and composed of a core plate, filling plate and restraint plate (Fig. 2a). The core plate was welded to the structural members and yielded under repeated axial loads. The filling plate and restraint plate were used to prevent compression buckling of the core plate. The section of the core plate varied along the length (Fig. 2b) and was divided into yielding segments, transition segments, and connection segments. In addition, the stable hysteretic energy-dissipation capacity of the REDC observed in an axial cyclic tension–compression test is given in Fig. 2c, d (Xie 2020). The damage to the connection was mainly concentrated in the yielding segment of the REDC core plate. The energy-dissipation capacity of the novel precast connection was provided by the tension and compression plastic deformation of the REDC core plate. After an earthquake, the structures can be repaired quickly by replacing the REDCs.

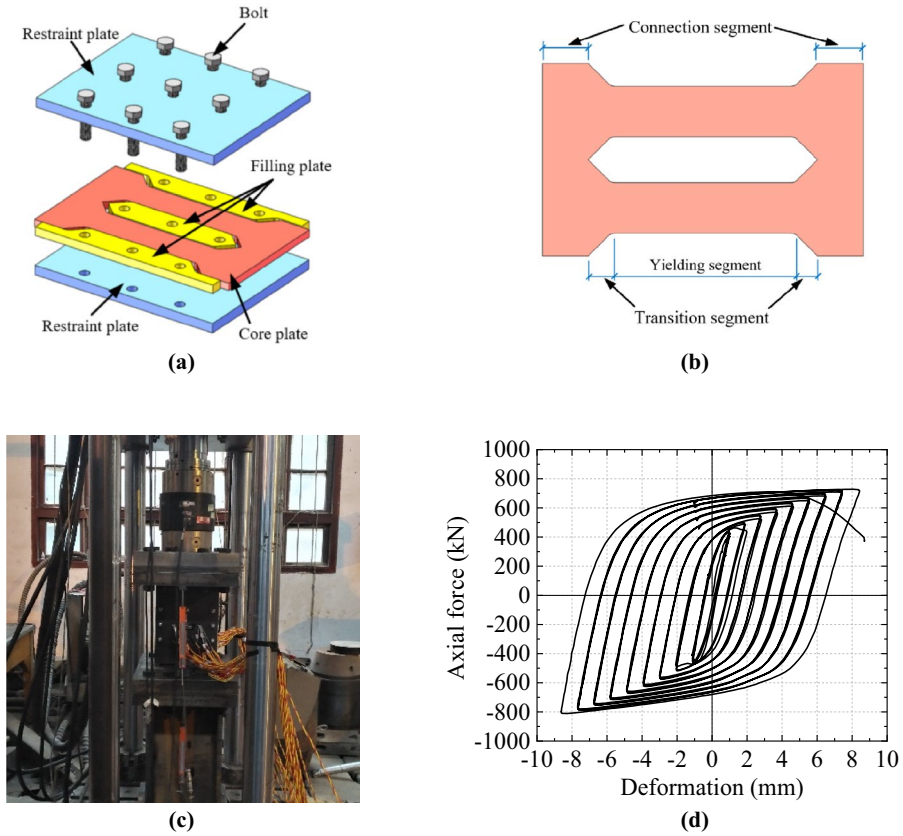


Fig. 2 Details and test of the REDC: **a** details of the REDC, **b** details of the REDC core plate, **c** test of the REDC, and **d** hysteric curve of the REDC

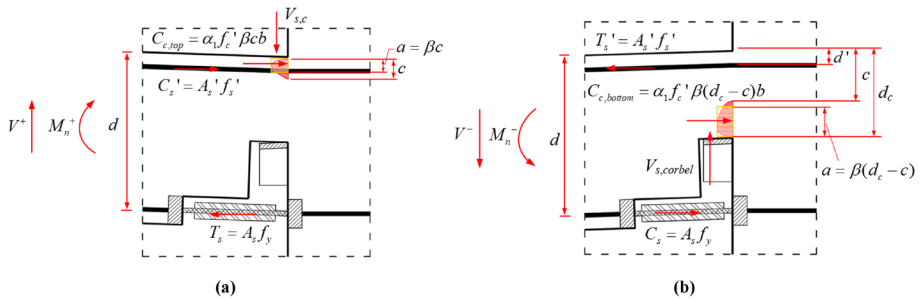


Fig. 3 Force distribution in the connection under positive and negative bending: **a** positive moment (gap opening) and **b** negative moment (gap closing)

2.3 Load-carrying mechanism

Figure 3a, b illustrate the forces in this novel precast connection under positive (gap opening) and negative (gap closing) bending moments. The flexural response of this novel precast connection was governed by the yielding of the REDC core plate and the concrete compression zone.

The positive bending moment of the novel connection ($M+n$) could be calculated similar to that in a conventional RC connection, i.e., by multiplying the REDC yield force about a lever arm, as indicated by Eq. (1). This is an approximation that conservatively ignores the force in the top reinforcements and any additional confinement to the concrete hinge from the column face.

$$M_n^+ = A_s f_y d - a/2 \tag{1}$$

where A_s represents the equivalent cross-sectional area of the REDC core plate, f_y represents the yield strength of the REDC core plate, d represents the beam effective depth, and a represents the Whitney equivalent rectangular concrete stress block depth.

The flexural mechanism for negative bending moments in this novel precast connection ($M-n$) differed from that in conventional RC beams. There was no concrete compression at the beam soffit owing to the slot. However, there was concrete compression at the bottom of the concrete top hinge, as shown in Fig. 3b. The negative bending moment can be accurately approximated as follows:

$$M_n^- = A_s f_y d - d' + \alpha_1 f_c' \beta (d_c - c) b (d_c - a/2 - d') \tag{2}$$

where d' represents the distance between the extreme top fiber and the centroid of the top longitudinal reinforcement, α_1 and β are concrete stress block factors, f_c' represents the specified 28-d concrete compressive strength, d_c represents the depth of the concrete top hinge in this novel precast connection, c represents the neutral-axis depth (measured from the top surface of the beam), and b represents the section width of the beam.

For gap-opening rotations (positive moment), the shear forces transferred through the compression concrete zone can be designed according to the Code for Seismic Design of Buildings in China (GB50010-2010) (2010) as follows:

$$V^+ \leq V_{s,c} = 0.25 \beta_c f_c' b h_0 \tag{3}$$

where $V_{s,c}$ is the shear force transferred through the compression concrete zone, β_c is the coefficient of the concrete strength (1.0 for C50 concrete), and h_0 represents the effective height of the cross-section (h_0 represents d_c in this novel precast connection).

For gap-closing rotations (negative moment), the shear forces transferred via the hidden corbel can be designed according to Eq. (4).

$$V^- \leq V_{s,corbel} \tag{4}$$

where $V_{s,corbel}$ represents the shear capacity provided by the hidden corbel.

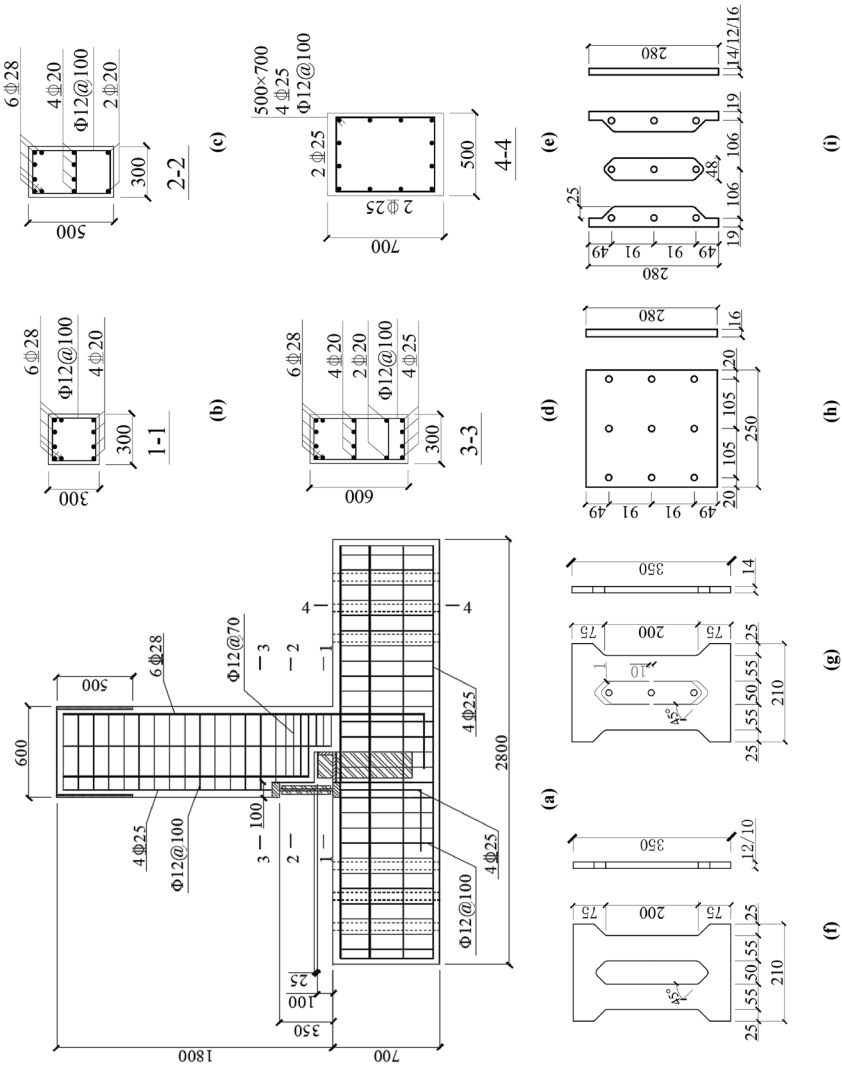


Fig. 4 Details of the tested connections (all dimensions are in units of mm): **a** dimensions and details of the specimen, **b** reinforcements of beam section 1-1, **c** reinforcements of beam section 2-2, **d** reinforcements of beam section 3-3, **e** reinforcements of column section 4-4, **f** dimensions and details of the core plate in Tests 1 and 2, **g** dimensions and details of the core plate in Test 3, **h** dimensions and details of the restraint plate, and **i** dimensions and details of filling plate

Table 1 Mechanical properties of the structural steels in the specimen

Material	Structural components	Yielding strength f_y (MPa)	Ultimate strength f_u (MPa)	Young's modulus E_s (N/mm ²)
Q345	Steel corbel and connecting blocks	443.98	586.32	211,023
HRB400	Reinforcement D28	420.18	490.04	206,734
HRB400	Reinforcement D25	417.21	478.92	206,837
HRB400	Stirrup 14	476.12	527.33	210,322

Table 2 Cube strength of C50 concrete

Test specimen	1	2	3	Average
Strength (MPa)	60.22	51.38	53.47	55.02

3 Experimental study on the novel precast connection

3.1 Test specimen

To experimentally investigate the hysteretic behavior of the novel precast connection under cyclic loading, a full-scale test specimen was fabricated, as shown in Fig. 4. This specimen corresponded to the exterior beam-to-column connection from a prototype concrete frame in China. According to GB50010-2010 (2010), this frame was located in an area of seismic intensity 8, seismic group 1, and soil type II, with a peak ground acceleration (PGA) of 0.4 g for the maximum considered earthquake (MCE) (2% exceedance probability in 50 years). As shown in Fig. 4a, the column was 2800 mm tall, with a cross-section with dimensions of 500 mm × 700 mm. The beam was 1800 mm long, with a cross-section of 300 mm × 600 mm. The cross-sections and reinforcement layouts of the beam and column are shown in Fig. 4b–e. The REDC was connected with the core plate, the restraint plates, and the filling plates using bolts. The dimensions and parameters of the REDCs are shown in Fig. 4f–i. There were 1-mm gaps between the filling plates, restraint plates, and core plate. There was a sufficient gap between the filling plates and the core plate to satisfy the compression deformation of the core plate. Note that there were two stoppers (10 mm) in the 14-mm core plate (i.e., Test 3), as shown in Fig. 4g. The stopper was a connection segment that connected the core plate and the restraint plate. Au (2010) proposed that when $A_s'f_y/A_s f_y > 2.5$, the neutral axis of the connection would move upward, and the top reinforcements would remain in the elastic range. Therefore, for the top longitudinal reinforcements in this novel precast connection, six 28-mm-diameter deformed bars and HPB400 steel (yield stress of 400 MPa) were used to decrease the yield-capacity ratio of the top reinforcements to the bottom REDC ($A_s'f_y/A_s f_y$). Note that these six bars included equivalent reinforcements in the slabs. Therefore, the flange effect of the slabs in the connection was considered by equivalent reinforcements. In addition, the thickness of the REDC core plate was 14 mm. Therefore, $A_s'f_y/A_s f_y$ for the test specimen was 3.68 (> 2.5). To simplify the construction of the specimen, the sleeve-connected top reinforcements were replaced with continuous reinforcements. One π -shaped steel hidden corbel was embedded in the column at the half-height of the beam. The length of the corbel was 80 mm, and the cross-section of the flange plate in the π -shaped steel corbel was 300 mm × 18 mm. The

cross-section of the web plates in the π -shaped steel corbel was 18 mm \times 160 mm. The width of the slot adjacent to the column face was 25 mm, which was sufficient to accommodate 4.0% drifts without contact between the beam soffit and the column face. The height of the slot (the distance from the top of the corbel to the bottom of the beam) was 300 mm.

3.2 Material properties

For the test specimen, the material properties of the reinforcements, π -shaped steel corbel and connecting blocks are presented in Table 1. Note that the data in Table 1 are the average values of the test results of the three specimens. The test results of the steel plate and reinforcements satisfied the Standard for Design of Steel Structures in China (GB50017-2017) (2017) and GB50010-2010 (2010), respectively.

The grade of the concrete in the specimen was C50. The compressive strength of the three cubic standard specimens (150 mm \times 150 mm) after 28 d of curing was tested, and the test results all satisfied GB50010-2010. The test results are presented in Table 2.

Three samples of the Q235 plate used to fabricate the REDC were tested. The test results are presented in Table 3.

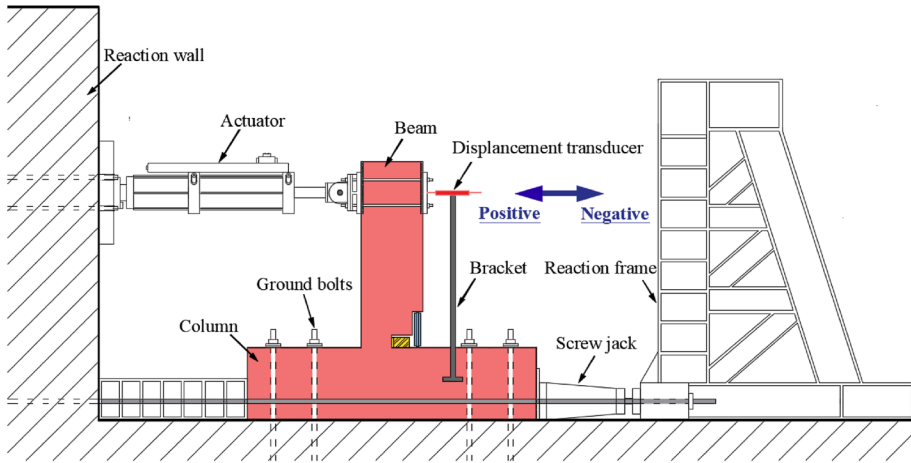
3.3 Test setup and loading protocol

The beam-to-column assembly was rotated of 90° for the test, and the test setup is shown in Fig. 5. A lateral load was applied near the beam end using an actuator with a scale of ± 1000 kN. A displacement transducer with a scale of ± 150 mm was installed at the bottom of the beam to record and calculate the relative rotation between the beam and the column during the tests. At the ends of the column, two jacks were used to apply an axial load, which corresponded to an axial compression ratio of 0.2, as recommended by GB50010-2010 (2010). At the same time, the horizontal slip of the specimen was limited by the two jacks. Additionally, two displacement transducers were placed at the same position to detect horizontal movement to enhance the accuracy of the measurements.

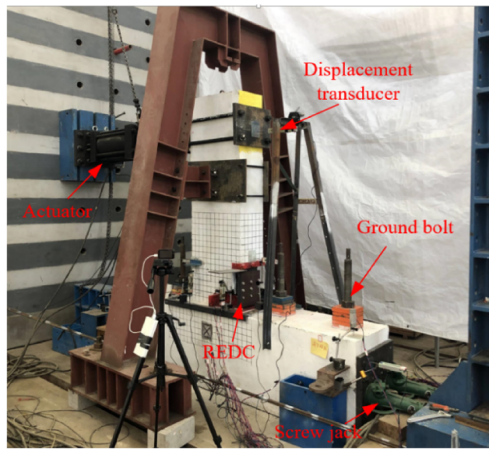
The drift sequence in Fig. 6 was adopted in accordance with the American Concrete Institute (ACI) acceptance criteria for moment frames (2005). The test specimens were subjected to three cycles at drift levels of 0.1%, 0.2%, 0.5%, 0.75%, 1.0%, 1.5%, 2.0%, 2.5%, 3.5%, and 4.5%. A smaller cycle (one-third of the previous drift) followed each large drift set to close the gaps between the aggregates in the concrete.

Table 3 Material test results for Q235 steel

No.	Yielding strength f_y (MPa)	Ultimate strength f_u (MPa)	Young's modulus E_s (N/mm ²)	Yield ratio (%)	Ductility (%)
A	271.29	458.43	211,468	59.18	38.51
B	262.31	456.30	214,452	57.49	39.42
C	270.26	460.65	212,122	58.67	39.55
Average	267.95	458.46	212,681	58.45	39.16



(a)



(b)

Fig. 5 The specimen under test: a test setup and instrumentations and b photograph of the specimen under test

Fig. 6 Quasi-static loading

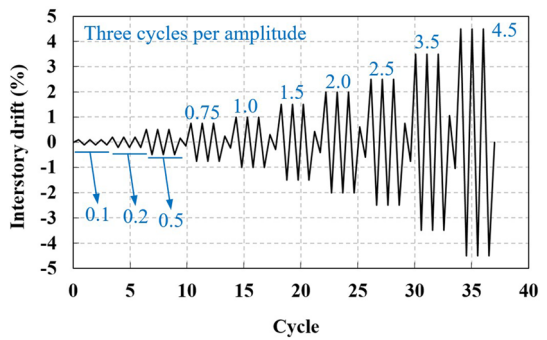


Table 4 Test matrix

Test number	Thickness of the core plate (mm)	Bolt parameters		Stopper	Unbonding Material
		Type	Size (mm)		
Test 1	12	4.8-grade	M12×60	–	N
Test 2	10	10.9-grade	M14×60	–	N
Test 3	14	10.9-grade	M14×60	10 mm	Y

3.4 Test matrix

The thickness of the REDC core plate and the structural details of the REDC were significant design parameters that affected the hysteretic responses of the novel precast connection. To investigate the seismic behaviors in the novel precast connection, a specimen was subjected to three tests with variations in the design parameters. The design parameters used for the tests are presented in Table 4. In Test 1, the thickness of the REDC core plate was 12 mm, and the core plate contained no stoppers or unbonding material. Note that the unbonding material was butyl rubber. Additionally, 4.8-grade M12×60 mm ordinary bolts were used to connect the REDC. In Test 2, the thickness of the REDC core plate was 10 mm, and the core plate contained no stoppers or unbonding material. Different from Test 1, 10.9-grade M14×60 mm high-strength bolts were used to connect the REDC in Test 2. In Test 3, the thickness of the REDC core plate was 14 mm, and the connection bolts were 10.9-grade M14×60 mm high-strength bolts. Different from Tests 1 and 2, the core plate in Test 3 had stoppers (two 10-mm-long connections) and unbonding material. The stoppers in Test 3 were used to fix the restraint plates and the filling plates in the center of the core plate to reduce the friction of the core plate and the restraint plates. Additionally, unbonding material was used to reduce the friction between the core plate and the restraint plates. The necking phenomenon of the core plate and the stress concentration were reduced by reducing friction.

4 Experimental results and discussion

4.1 Hysteretic response

The hysteretic responses of the three tests are shown in Fig. 7. In all the tests, failure occurred via the fracture of the REDC core plate owing to low-cyclic fatigue. The drift ratios were calculated by dividing the displacement at the tip of the beam by the shear span (the shear span was 1500 mm). The drift ratio in the hysteretic response (Fig. 7) was the relative drift of the beam and column and was measured by the displacement transducer fixed on the column (shown in Fig. 5a). Therefore, the drift ratio of the hysteresis response in Fig. 7 was authentic and fully showed the true hysteresis performance of this novel precast connection. It could be clearly seen that the drift ratio in the hysteretic curve was smaller than that in the loading protocol due to the gap between the actuator and the specimen and the slight slip in the loading process. In addition, as shown in Fig. 7a, the positive and negative drifts of Test 1 differed at the same drift level. Additionally, the negative drift in the Test 1 hysteretic curve (Fig. 7a) was smaller than the drift in the loading protocol.

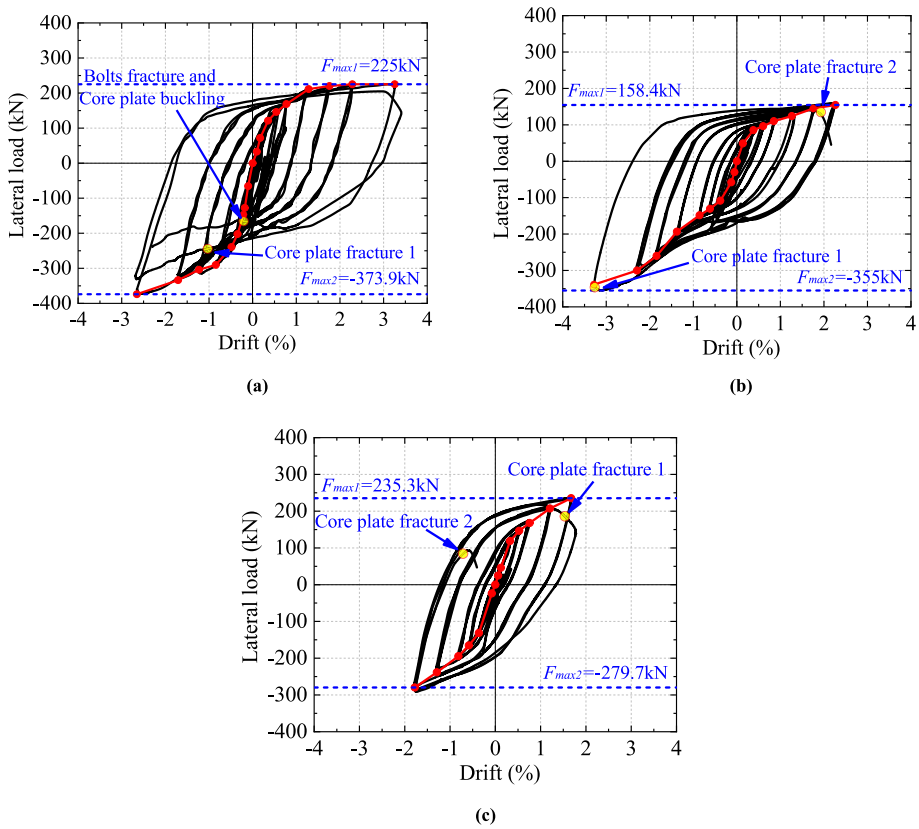


Fig. 7 Load versus drift response for the novel beam-to-column precast concrete connection: **a** Test 1 (10 mm), **b** Test 2 (10 mm), and **c** Test 3 (14 mm)

Table 5 The results of the three tests

Test number	θ_{max1} (%)	F_{max1} (kN)	θ_{max2} (%)	F_{max2} (kN)	$\theta_{f1,level}$ (n_{f1}) (%)	$\theta_{2,level}$ (n_{f2}) (%)
Test 1	3.41	225	-2.69	-373.9	3.5 (2nd cycle)	3.5 (3rd cycle) ^a
Test 2	2.24	158.4	-3.28	-355	3.5 (1st cycle)	3.5 (3rd cycle)
Test 3	1.8	235.3	-1.81	-279.7	2.0 (3rd cycle)	2.0 (4th cycle)

$\theta_{f1,level}$ and $\theta_{f2,level}$ are the drift level in the loading protocol corresponding to the two side of the REDC core plate fractured; n_{f1} and n_{f2} are the number of the cycles at $\theta_{f1,level}$ and $\theta_{2,level}$ respectively

^a The drift corresponding to the REDC core plate buckling in Test 1 due to the fracture of the ordinary bolts

This was attributed to the rigid-body rotation and slippage of the specimen during the negative drift due to anchor failure of the two ground bolts on the left side of the specimen. To prevent this phenomenon from occurring in Test 2 and Test 3, the two anchor-failed ground bolts were refastened after Test 1, and a stronger torsional moment was applied to the ground bolts. The maximum positive drift (θ_{max1}), maximum negative drift (θ_{max2}), maximum positive force (F_{max1}), maximum negative force (F_{max2}), drift level in the loading protocol corresponding to the first fractured side of the REDC core plate ($\theta_{f1,level}$), drift

level in the loading protocol corresponding to the second fractured side of the REDC core plate ($\theta_{f2,level}$), number of cycles at $\theta_{f1,level}$ (n_{f1}), and number of cycles at $\theta_{f2,level}$ (n_{f2}) are summarized in Table 5.

In Test 1, as shown in Fig. 7a, θ_{max1} was 3.41% (the corresponding θ_{level} in the loading protocol was 3.5%), and F_{max1} was 225 kN, corresponding to the first cycle at this drift level. θ_{max2} was -2.69% (the corresponding θ_{level} in the loading protocol was -3.5%), and F_{max2} was -373.9 kN, corresponding to the first cycle at this drift level. One side of the REDC core plate fractured at -1.03% drift (during the second cycle at the -3.5% drift level). In addition, the REDC core plate buckled at -0.21% drift (during the third cycle at the -3.5% drift level) because ordinary bolts connected the restraint plates and the filling plates fractured.

In Test 2, as shown in Fig. 7b, θ_{max1} was 2.24% (the corresponding θ_{level} in the loading protocol was 2.5%), and F_{max1} was 158.4 kN, corresponding to the first cycle at this drift level. θ_{max2} was -3.28% (the corresponding θ_{level} in the loading protocol was -3.5%), and F_{max2} was -355 kN, corresponding to the first cycle at this drift level. One side of the REDC core plate fractured when the loading drift increased to -3.27% (during the first cycle at the -3.5% drift level), and the other side of the REDC core plate fractured when the loading drift increased to 1.93% (during the first cycle at the 3.5% drift level).

In Test 3, as shown in Fig. 7c, θ_{max1} was 1.8% (the corresponding θ_{level} in the loading protocol was 2.0%), and the corresponding F_{max1} was 235.3 kN. θ_{max2} was -1.81% (the corresponding θ_{level} in the loading protocol was -2.0%), and the corresponding F_{max2} was -279.7 kN. One side of the REDC core plate was fractured when the loading drift increased to 1.54% (during the third cycle at the 2.0% drift level), and the other side of the REDC core plate was fractured when the loading drift increased to -0.71% (during the fourth cycle at the -2.0% drift level).

There were two main explanations for the differences in the bearing capacity at the same drift in the three tests. First, the thickness of the REDC core plate had a strong influence on the bearing capacity of the connection. With increasing core plate thickness, the bearing capacity of the connection increased. Second, the differences in the three test results must have been influenced by the damage in the concrete compression zone. In Test 1, the specimen was in a damage free state. In Tests 2 and 3, the concrete compression zone was

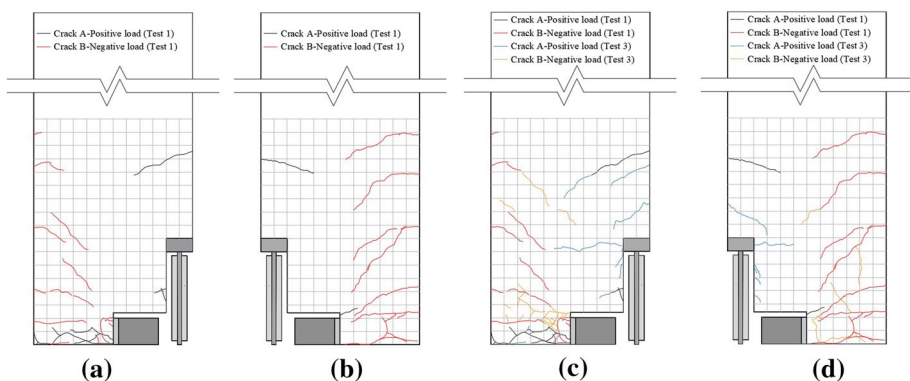


Fig. 8 Cracking patterns at the ultimate condition: **a** Test 1 (front elevation), **b** Test 1 (back elevation), **c** Test 3 (front elevation), and **d** Test 3 (back elevation)

damaged before loading. Both of these ideas are described in detail in Sect. 4.5 (Skeleton curve).

As shown in Fig. 7, the loading drift in Test 3 was smaller than those in Tests 1 and 2 due to the discreteness of the steel. The fatigue performance of the steel used for the REDC core plate in Test 3 was worse than that in Tests 1 and 2. In addition, the difference could be attributed to the initial defect in the core plate caused by wire electrical discharge machining (WEDM) technology, described in detail in Sect. 4.3 (Failure mode).

4.2 Cracking pattern

The cracking patterns of the front and back elevations in Test 1 are shown in Fig. 8a, b, respectively. Compared with Test 1, there were almost no new cracks in Test 2, and only a few of the original cracks continued to expand. This was attributed to the fact that the thickness of the core plate in Test 2 was smaller than that in Test 1, so the loading capacity of Test 2 was smaller than that in Test 1. In view of this, the cracking pattern in Test 2 is not presented. The cracking patterns of the front and back elevations in Test 3 are shown in Fig. 8c, d, respectively.

As shown in Fig. 8, the cracks, including shear cracks and the flexural cracks, were mainly concentrated in the top hinge of the beam. The cracks were divided into two types: crack A under positive drift and crack B under negative drift. Figure 9 shows photos of the cracking patterns at the ultimate condition.

In Test 1, the first crack occurred in the beam near the beam–column interface at a drift of -0.1% . With increasing loading drift (to 0.2% , 0.5% , and 1.0%), under positive loading, flexural cracks (crack A) developed in the lower part of the beam, and under negative loading, flexural cracks (crack B) developed in the upper part of the beam away from the beam–column interface. Some of the flexural cracks developed quickly at the top of the beam and connected with the cracks at the back of the beam, forming through-cracks; these were the main cracks of the connections. As the loading drift increased to 1.0% and 1.5% , shear cracks developed in the upper part of the beam, gradually developing from the upper part of the hidden corbel and extending into the plastic hinge zone. When the loading drift reached 1.5% , the interface of the hidden corbel and the beam was opened. As the drift increased further (to 2.0% , 2.5% , and 3.5%), the concrete spalled in the upper part

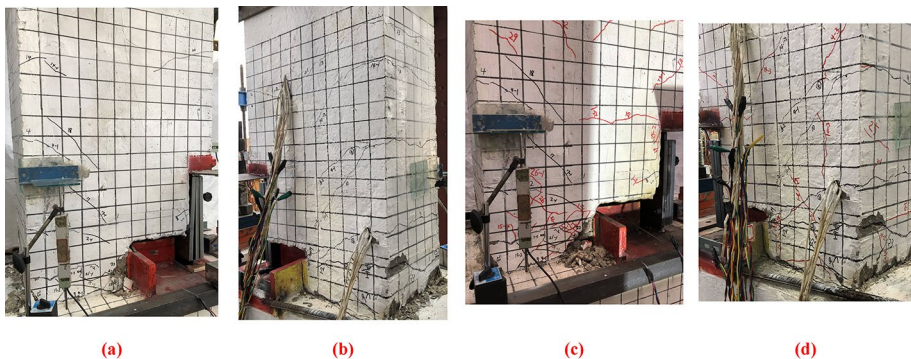


Fig. 9 Photos of the cracking patterns at the ultimate condition: **a** Test 1 (front elevation), **b** Test 1 (back elevation), **c** Test 3 (front elevation), and **d** Test 3 (back elevation)

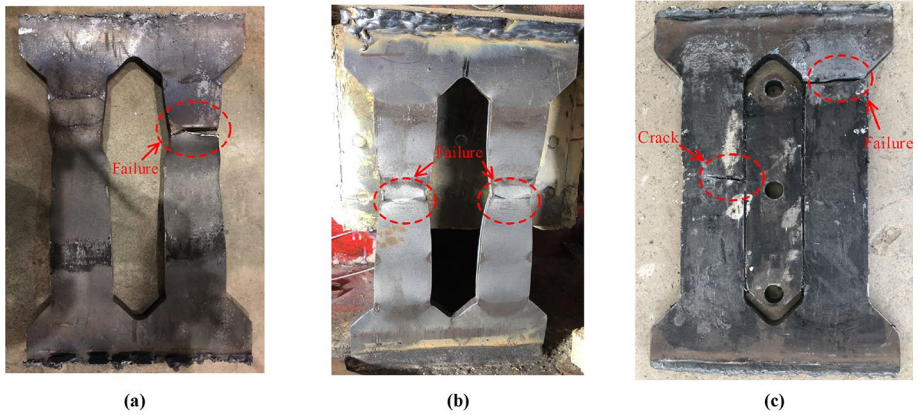


Fig. 10 Failure pattern of the core plate: **a** Test 1 (12 mm), **b** Test 2 (10 mm), and **c** Test 3 (14 mm)

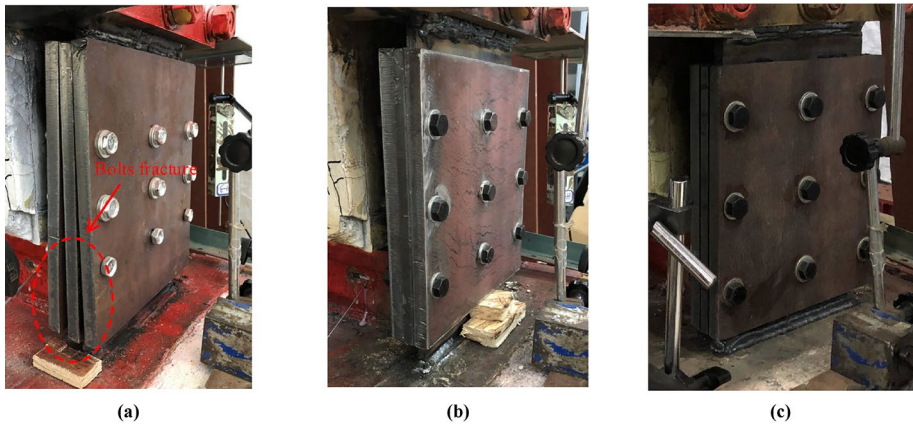


Fig. 11 Buckling restraint state of the REDC: **a** Test 1 (12 mm), **b** Test 2 (10 mm), and **c** Test 3 (14 mm)

of the corbel and the top of the beam near the beam–column interface owing to compression damage. New shear cracks and flexural cracks appeared under the larger loading drift because of the increase in the bending moment and the shear force in Test 3. However, note that the trend of the crack development in Test 3 was similar to that in Test 1.

4.3 Failure mode

As shown in Fig. 10a, the fracture of the REDC core plate in Test 1 was located in the yielding segment of the core plate, where one crack formed. The REDC core plate was fractured because of the large strain at the low-cycle fatigue. Because no unbonding material was used in Test 1, necking occurred in the REDC core plate, and several scratches were clearly observed on the core plate due to the friction between the core plate and the

restraint plate. The ordinary bolts (4.8-grade) connected the restraint plates, and the filling plates were fractured, as shown in Fig. 11a.

As shown in Fig. 10b, necking occurred in the REDC core plate, and several scratches caused by the friction between the core plate and the restraint plate were clearly observed on the core plate because no unbonding material was used in Test 2. The fracture of the REDC core plate in Test 2 was located in the yielding segment of the core plate, where two cracks formed. Because high-strength bolts were used in Test 2, the REDC core plate was effectively protected from buckling by the restraint plates, as shown in Fig. 11b.

As shown in Fig. 10c, no scratches were observed in the REDC core plate because stoppers and unbonding material were used in Test 3. Additionally, no necking phenomena were observed in the REDC core plate. Moreover, the REDC core plate in Test 3 fractured at the junction of the yielding segment and the transition segment. On the other side, a crack was formed at the middle of the yielding segment of the core plate (near the stopper). The drift in Test 3 was smaller than that in Tests 1 and 2, which was attributed to an initial defect in the core plate caused by WEDM. The WEDM technology used to realize the two 10-mm stoppers and a 1-mm gap between the core plate and the filling plate readily caused an initial defect in the core plate. This initial defect led to early failure of the REDC, which limited the ductility of the REDC. This could be proven by the lack of obvious necking in the REDC core plate and its unique failure location. In addition, because high-strength bolts (10.9-grade) were used in Test 3, the REDC core plate was effectively protected from buckling by the restraint plates, as shown in Fig. 11c.

As shown in Fig. 12, two waves were formed in the yielding segment of the REDC core plate by weak axis multiwave buckling. Figure 12a and b are schematic diagrams of the REDC core plate buckling in Test 1 and in Tests 2 and 3, respectively. Note that the buckling amplitude of the REDC core plate in Test 1 was slightly larger than those in Tests 2 and 3 ($\delta_1 > \delta_2$) due to the fractured ordinary bolts.

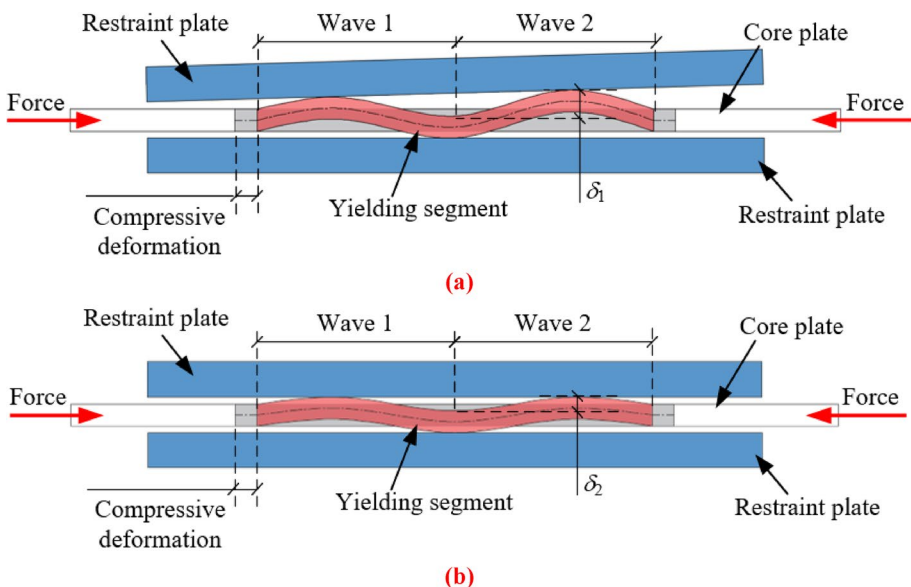
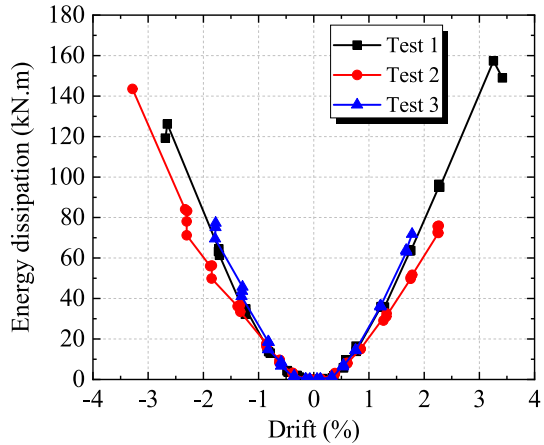


Fig. 12 Multi-wave buckling of the REDC core plate: aTest 1 (12 mm) and bTests 2 and 3 (10/14 mm)

Fig. 13 Energy dissipation per cycle versus drift ratio

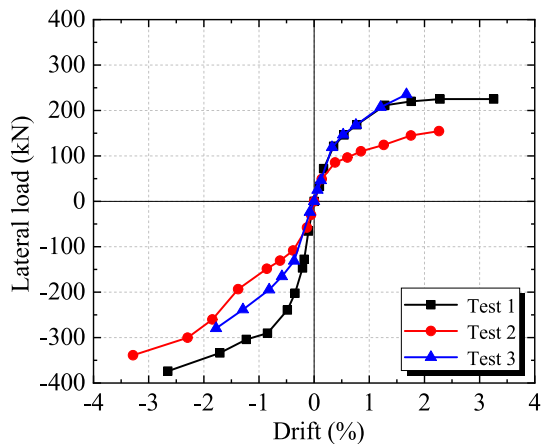


4.4 Energy dissipation

The energy-dissipation capacity is an important index for evaluating the seismic behavior of structures. The energy dissipation per cycle, defined as the area enclosed by a load–displacement cycle, was used to evaluate the energy dissipation of the novel precast connection. The energy dissipation per load cycle under positive and negative drifts was examined, and the energy dissipation of the smaller cycles and the incomplete final cycles was neglected, as shown in Fig. 13.

With gap opening and closing, the energy dissipation per cycle of the novel precast connection exhibited an almost symmetrical “V” shape, as shown in Fig. 13. In the three tests, the energy dissipation per cycle was relatively small when the drift ratio was small (<0.5%). However, it increased significantly with increasing drift ratio. As indicated by Fig. 13, the energy dissipation per cycle in Test 3 (under both the positive and negative drifts) was slightly greater than that in Test 1, and the energy dissipation per cycle in Test 1 was greater than that in Test 2. The results suggested that the energy dissipation per cycle of the novel precast connection increased with the thickness of the REDC core plate.

Fig. 14 Skeleton curve



Additionally, the difference in the energy dissipation per cycle between Tests 2 and 1 was greater than that between Tests 3 and 2, which was attributed to the energy-dissipation capacity of the novel precast connection in Test 1 not only provided by the REDC but also provided by the concrete crushing between the beam–column surfaces. However, in Tests 2 and 3, the energy-dissipation capacity of the novel precast connection was provided by the REDC only because the plastic hinge of the specimen was fully formed after Test 1. Finally, as shown in Fig. 13, the energy-dissipation values per cycle under the same positive and negative drift levels were approximate, indicating that the energy-dissipation capacity of the novel precast connection was excellent under both positive and negative bending moments.

4.5 Skeleton curve

The skeleton curves of the three tests are presented in Fig. 14. As shown in Fig. 14, the negative force was greater than the positive force at the same drift, and the discrepancy was more significant in Tests 1 and 2 than in Test 3. Although the thickness of the REDC core plate in Test 1 was smaller than that in Test 3, the positive force of Test 3 was very close to that of Test 1 at the same positive drift, which was attributed to the contribution of the concrete compression zone in Test 1. In addition, the positive force in Test 1 was greater than that in Test 2 due to the difference in the REDC core plate thickness. Additionally, in Tests 2 and 3, the plastic hinge was completely formed, and the concrete compression zone no longer provided compressive stress. It could be concluded that the bearing capacity of the novel precast connection was directly influenced by the parameters of the REDC.

Additionally, at the same negative drift, the negative force in Test 1 was greater than that in Test 2, and the negative force in Test 2 was greater than that in Test 3. In addition, the difference in the negative force between Tests 1 and 2 was greater than the difference in the negative force between Tests 2 and 3. This most likely occurred because the compressive stress provided by the concrete compression zone caused the top reinforcements to yield at the initial loading process, and then the bearing capacity of the connection increased rapidly. As mentioned previously, the plastic hinge was completely formed in Test 1. The concrete compression zone no longer provided compressive stress in Tests 2 and 3. Another important factor was that the yield stress of the top reinforcements increased due to the “cold drawing” effect after loading in Test 1, which delayed the yielding of the top

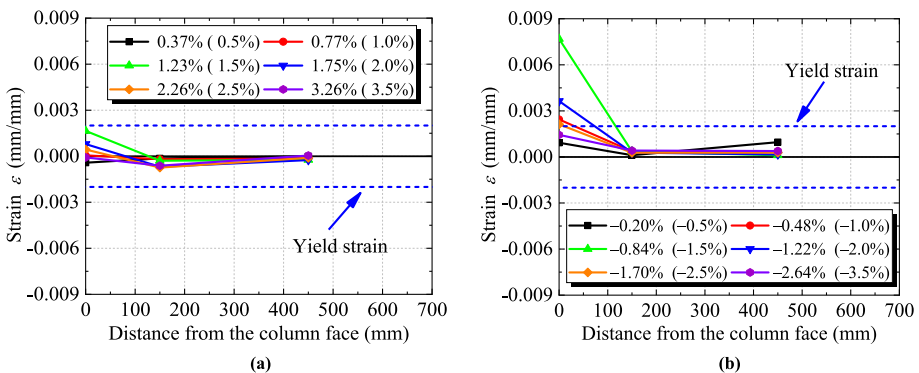


Fig. 15 Strain profiles of the top reinforcement in Test 1: **a** positive drifts and **b** negative drifts

reinforcements (increased the yield strain of the top reinforcements) compared with that in Test 1. The “cold drawing” effect means that the yield stress and strain of the reinforcement after tensile yield are higher than those of the initial state. Additionally, the thickness of the REDC core plate in Test 2 decreased, making the bearing capacity in Test 2 lower than that in Test 1. The yield stress and strain of the top reinforcements in Test 3 were further increased due to the second “cold drawing” effect in Tests 2. Combined with the fully developed plastic hinge, the bearing capacity in Test 3 was lower than that in Test 1, although the thickness of the core plate increased.

4.6 Top longitudinal reinforcement strain profile

The strain of the top reinforcement was accumulated in the three tests because the three tests were successively performed on a single novel precast connection specimen. Therefore, the top longitudinal reinforcement strain in Test 1 was the key to this study. Figure 15a and b show the peak strain of the top longitudinal reinforcement at each peak positive and negative drift, respectively. Additionally, the actual peak drift of each cycle is shown in the legend, and the corresponding drift in the loading protocol is shown in brackets.

As shown in Fig. 15, the variation in the top reinforcement strain was the largest at 0 mm from the column face, and the reinforcements yielded. The top reinforcement strains at 150 and 450 mm were small and remained in the elastic range. The top reinforcements remained in the elastic range under positive drift (Fig. 15a) and yielded under negative drift (Fig. 15b). In addition, some tensile strains during gap-opening rotations were exhibited when compression was expected. This was most likely the result of larger residual tensile strains from previous gap-closing cycles, allowing compressive stresses to occur at positive strains.

Equations (5) and (6) are force balance formulas of the connection. After expansion and transformation, Eqs. (7) and (8) can be obtained:

$$T'_s = C'_s + C_{c,bottom} \quad (5)$$

$$T_s = C'_s + C_{c,top} \quad (6)$$

$$A'_s f'_s = A_s f_y + \alpha_1 f'_c \beta (d_c - c) b \quad (7)$$

$$A_s f_y = A'_s f'_s + \alpha_1 f'_c \beta c b \quad (8)$$

With increasing negative drift, the compression of the REDC (C_s) and the concrete compression zone ($C_{c,bottom}$) both increased continuously (Eq. (5)). Although $A_s f'_y / A_s f_y = 3.68$ (> 2.5) in the specimen, the compression force provided by the concrete compression zone ($C_{c,bottom}$) was very large. Therefore, the tensile stress of the top longitudinal reinforcements quickly increased until the top reinforcements yielded. Under positive drift, the compression (C'_s) provided by the top longitudinal reinforcements and the compression ($C_{c,top}$) provided by the concrete compression zone worked together to counteract the tension (T'_s) provided by the REDC, as shown in Eq. (6). Owing to the limited strain hardening of the REDC core plate and that $A_s f'_y / A_s f_y = 3.68$ (> 2.5), the top reinforcements remained in the elastic range under positive drift.

4.7 Additional bending moment

The additional bending moment was an important cause of connection damage. The additional bending moment of the connection was also a major obstacle to the formation of the "strong column and weak beam" mechanism, causing issues in the design. Therefore, in this novel precast connection research, the control of the bending moment of the connection was pursued through the reduction of the additional bending moment.

The bending moment of the conventional beam-to-column connection was produced by the combined action of the compression provided by the concrete compression zone and the top/bottom reinforcements and the tension provided by the bottom/top reinforcements. If the top and bottom reinforcements in the beam are the same, the positive and negative bending moments are as shown in Eq. (9). Then, the additional bending moment (M_{add}) produced by the combined action of the compression force generated by the concrete compression zone and the tension force generated by the top/bottom reinforcements can be expressed by Eq. (10).

$$M_n^\pm = A_s f_y d - d' + \alpha_1 f_c' \beta (d - c) b (d - a/2) \tag{9}$$

$$M_{add} = \alpha_1 f_c' \beta (d - c) b (d - a/2) \tag{10}$$

The thickness of the concrete compression zone in the novel beam-to-column connection was decreased by means of a vertical slot, thereby reducing M_{add} . With this structural form, the positive and negative bending moments of the novel connection were governed by the yielding of the REDC core plate, realizing the design goal of a controllable bending moment in the connection. However, Eq. (2) shows that the novel beam-to-column connection still experienced M_{add} under negative drift. The M_{add} value of the novel beam-to-column connection proposed in this paper ($M_{add,novel}$) can be expressed by Eq. (11):

$$M_{add,novel} = \alpha_1 f_c' \beta (d_c - c) b (d_c - a/2) \tag{11}$$

Compared with Eq. (10), the $M_{add,novel}$ of the novel beam-to-column connection was significantly smaller than the M_{add} of the conventional beam-to-column connection because the height of the vertical slot was half of the beam height (i.e., $d_c < d$).

Fig. 16 Schematic diagram of additional bending moment

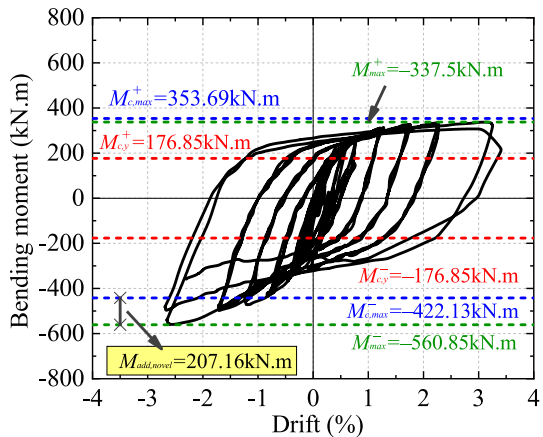


Figure 16 is an illustration of the $M_{add,novel}$ discussion with the example of Test 1. $M+c,y$ and $M-c,y$ are the positive and negative yield bending moments calculated by multiplying the yield force of the REDC about a lever arm, called the controllable yield bending moment, as shown in Eqs. (12) and (13), respectively. $M+c,max$ and $M-c,max$ are the overstrength bending moment values of the REDC (considering the strain hardening of the REDC), calculated by multiplying $M+c,y$ and $M-c,y$ by an overstrength factor, as shown in Eqs. (14) and (15), called the maximum controllable bending moment. The overstrength coefficient of the REDC under tension was conservatively taken as 2.0. Considering that the REDC was essentially a buckling-restrained brace (BRB), the compression force of the REDC was higher than the tension force due to the friction between the core plate and the restraint plate. Therefore, the overstrength coefficient of the REDC under compression was conservatively taken as 2.5. When M_{add} was zero, the height of the vertical slot in the connection was close to $d=h-(d'+d_{rein}/2)$, where h represents the height of the beam and d_{rein} represents the diameter of the top longitudinal reinforcement. In addition, the resultant concrete compression zone could be approximately considered to be near the center of the reinforcements under a positive bending moment. Therefore, $a/2$ in Eqs. (12) and (14) could be approximately replaced by d' . In addition, $M+max$ and $M-max$ were the maximum positive and negative bending moments of the specimen in Test 1, respectively. $M+c,y$, $M-c,y$, $M+c,max$, $M-c,max$, $M+max$, $M-max$, and $M_{add,novel}$ are summarized in Table 6.

$$M_{c,y}^+ = A_s f_y d - a/2 \quad (12)$$

$$M_{c,y}^- = A_s f_y d - d' \quad (13)$$

$$M_{c,max}^+ = A_s f_y \times 2 \times d - a/2 \quad (14)$$

$$M_{c,max}^- = A_s f_y \times 2.5 \times d - d' \quad (15)$$

Figure 16 shows that $M+max$ was very close to $M+c,max$, indicating that the positive bending moment of the novel beam-to-column connection was governed by the yielding of the REDC. In other words, the positive bending moment of the novel beam-to-column connection could be considered a controllable variable. However, $M-max$ was larger than $M-c,max$ (the extra part was M_{add}), indicating that the negative bending moment of the novel beam-to-column connection was not completely governed by the yielding of the REDC, and the extra part was governed by the compression force generated by the concrete compression zone. This feature can also be clearly seen from Eq. (2).

5 Finite element analyses

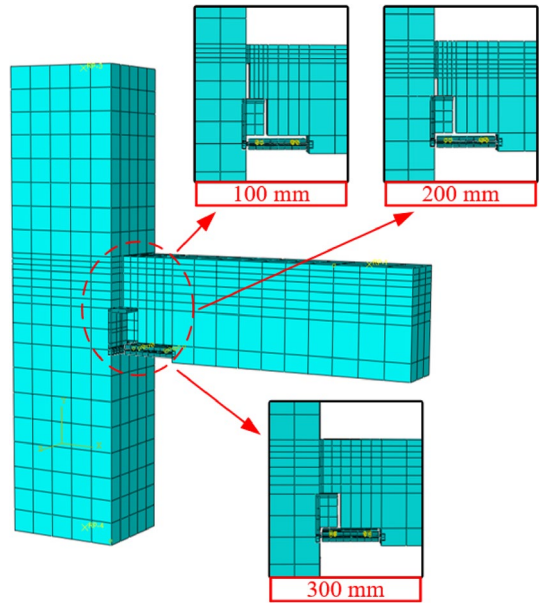
5.1 General

Au (2010) proposed that to keep the top reinforcement in the elastic range, $A_s f_y' / A_s f_y$ must be greater than 2.5. In view of this, the $A_s f_y' / A_s f_y$ in the novel precast connection test

Table 6 The critical bending moments of the novel beam-to-column connection in Test 1

$M + c,y$ (kN.m)	$M + c,max$ (kN.m)	$M + max$ (kN.m)	$M -c,y$ (kN.m)	$M -c,max$ (kN.m)	$M -max$ (kN.m)	$M_{add,novel}$ (kN.m)
176.85	353.69	337.5	-176.85	-442.13	-560.85	207.16

Fig. 17 ABAQUS model for the novel precast connection



specimen was designed to be 3.68 (>2.5). However, during the loading process, the top longitudinal reinforcements still yielded. Based on the analysis results of Sects. 4.6 and 4.7, a method was proposed to decrease the top longitudinal reinforcement strain and additional bending moment under negative drift by increasing the height of the slot (decreasing the thickness of the concrete compression zone). Additionally, this method was verified by finite element simulations.

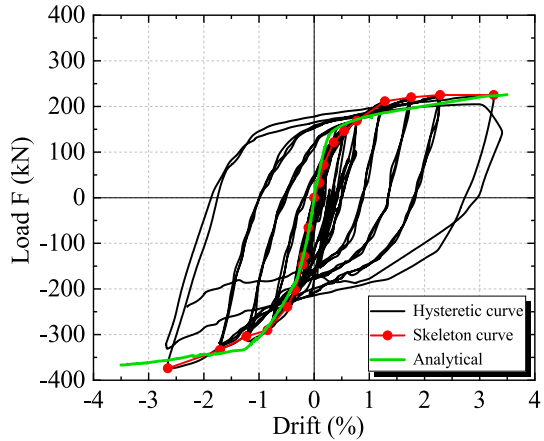
Numerical analyses were performed using ABAQUS, as shown in Fig. 17. The concrete, steel corbel, and REDC were modeled by eight-node three-dimensional (3D) linear brick elements with reduced integration (C3D8R), and the reinforcements were modeled by two-node 3D linear truss elements (T3D2). The reinforcements were embedded in the concrete. Surface-to-surface hard contact interaction was applied to the interface between the steel corbel and the precast beam, and the friction coefficient was assumed to be 0.35. All the geometric dimensions of the model were identical to those of the test specimen. The boundary conditions of the connection in the model were identical to those in the test. The depths of the top hinge in the three models were 300 mm ($d/d=1/2$), 200 mm ($d/d=1/3$), and 100 mm ($d/d=1/6$). To simplify the model and to identify the factors influencing the

Table 7 The major material parameters for concrete in ABAQUS

E_c (MPa)	ν_c	ψ	e	f_{b0}/f_{c0}	K	Viscosity coefficient
35,038.2	0.2	38	0.1	1.16	0.66666667	1E-005

E_c is the elastic modulus; ν_c is the Poisson’s ratio; ψ is the dilation angle; e is the flow potential eccentricity; f_{b0}/f_{c0} is the ratio of compressive strength under biaxial loading to uniaxial compressive strength and K is the ratio of the second stress invariant on the tensile meridian to that on the compressive meridian

Fig. 18 Comparison of analytical and experimental results



top longitudinal reinforcement strain, a pushover analysis was performed on each model. It was assumed that the REDC would not fail, i.e., could still function, at a drift ratio of 3%.

A bilinear kinematic hardening model considering the stiffness degradation of steel was used to simulate the steel corbels, reinforcements, and REDC. The elastic modulus was E when the bilinear kinematic hardening model was in the elastic stage. The hardening modulus was set as ηE when the model was in the elastoplastic stage, and η equaled 0.01. All the parameters in the bilinear kinematic hardening model were set according to the test results of the structural steels in the specimen (Tables 1 and 3). The damage plasticity model for concrete in ABAQUS was utilized to simulate the concrete. The major material parameters for confined and unconfined concrete in ABAQUS are listed in Table 7.

Figure 18 compares the response of the 300 mm analytical model with the experimental response of Test 1. The finite element simulation was compared with the skeleton curve because the finite element model was used in the pushover analysis. The result indicated that the elements were capable of accurately modeling the global force-drift response of the subassembly.

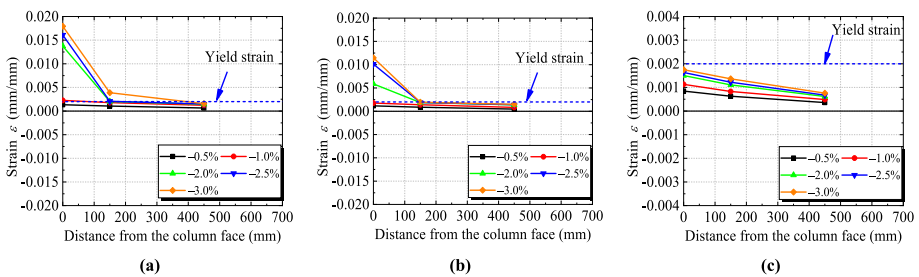


Fig. 19 The peak strain of the top longitudinal reinforcement corresponding to each negative peak drift in the three models: **a** Strain profile in top reinforcement at the negative peak drifts (300 mm), **b** Strain profile in top reinforcement at the negative peak drifts (200 mm), and **c** Strain profile in top reinforcement at the negative peak drifts (100 mm)

5.2 Decrease in the top longitudinal reinforcement strain under negative drift

To improve the reparability of the beam-to-column connection, the damage should be concentrated in the REDC as much as possible. In view of this, the DAD approach helped keep the top reinforcement in the elastic range as much as possible. In addition, the test results showed that the top reinforcement remained in the elastic range under positive drift but yielded under negative drift. Therefore, the effectiveness of increasing the vertical gap height to reduce the strain in the top reinforcements under negative drift was discussed based on the three finite element models.

The strain in the top longitudinal reinforcement at each negative peak drift in the three models is presented in Fig. 19. The strain profiles of the top longitudinal reinforcement in the three models were similar to the test results. The variation in the top reinforcement strain was the largest at 0 mm from the column face. The variations in the top reinforcement strains at 150 and 450 mm were relatively small. A comparison of Fig. 19a–c showed that the top reinforcement strain decreased with increasing slot height (decreasing top-hinge depth). In the model with a 500 mm slot height (100 mm top-hinge depth), the strain in the top reinforcement corresponding to negative drifts remained in the elastic range. As shown in Fig. 19a–c, with decreasing top-hinge depth (increasing vertical slot height), the top longitudinal reinforcement strain decreased significantly. When the top-hinge depth was 100 mm ($d_c/d = 1/6$), the top reinforcement remained in the elastic range. However, this value was smaller than the value of $d_c/d = 1/4$ recommended by Au (2010).

5.3 Decrease in the additional bending moment under negative drift

Figure 20 shows a comparison of the bending moments of the three models. It can be clearly seen that the negative bending moment of the connection decreases with increasing vertical slot height (decreasing top-hinge depth). When the top-hinge depth was 100 mm (vertical slot height was 500 mm), M_{max}^- was close to $M_{c,max}^-$. This result confirmed that when the vertical slot height increased to a certain value, the positive and negative bending moments of the novel connection were controllable. In other words, the positive and negative bending moments of the novel beam-to-column connection could be governed by the yielding of the REDC.

Fig. 20 The comparison of the bending moment

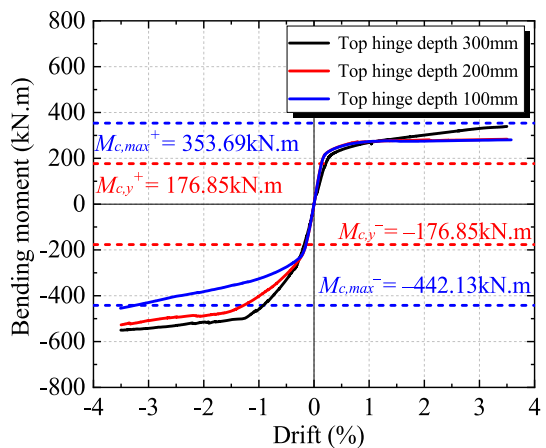
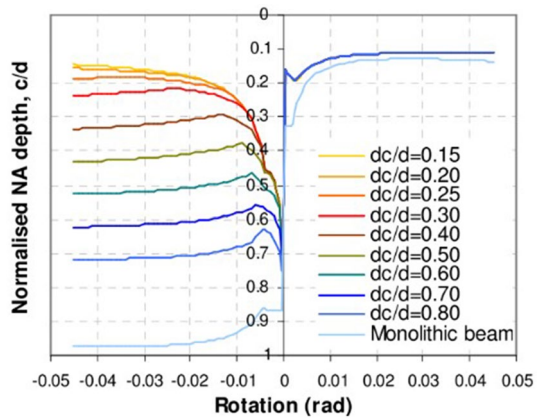


Fig. 21 Parametric study for the concrete top-hinge depth (Au 2010)



6 Recommended design value of the top-hinge depth

To obtain the recommended design value for the top-hinge depth, further theoretical analysis of the model was needed. The neutral-axis depth was affected by the height of the vertical slot. When the top-hinge depth decreased sufficiently, the neutral axis was infinitely close to the top longitudinal reinforcement of the novel precast connection. According to the force balance relationship (Eq. 7), the position of the neutral axis must be below the top longitudinal reinforcement. As shown in Fig. 21, when the top-hinge depth varied from $0.15d$ to $0.3d$, the position of the neutral axis was close to the top longitudinal reinforcement. Thus, the thickness of the concrete compression zone ($d_c - c$) was close to the height of the concrete below the top longitudinal reinforcement in the top hinge ($d_c - d' - d_{rein}/2$). Therefore, in the determination of the thickness of the concrete compression zone and the development of a formula for calculating the height of the beam hinge, it was conservative to consider the neutral-axis position as the position of the lower edge of the top longitudinal reinforcement. When the material properties and geometric dimensions of the connection were known, the safe (maximum) top-hinge depth for ensuring that the top longitudinal reinforcement remained in the elastic range can be calculated with Eq. (16):

$$d_c = (A'_s f'_y - A_s f_y \gamma) / \phi \alpha_1 f'_c \beta b + c \tag{16}$$

where γ is the strain hardening coefficient of the REDC. According to this assumption, c is the distance from the lower edge of the top longitudinal reinforcement to the top surface of the beam, i.e., $(d' + d_{rein}/2)$. When the top-hinge depth was less than or equal to the d_c obtained via Eq. (16), the top longitudinal reinforcement did not yield. Considering the increase in the concrete compression stress due to the confined influence of stirrups (Popovics 1973; Mander et al. 1988), the amplification coefficient ϕ was introduced in Eq. (16). Mander et al. (1988) proposed that the compressive strength of confined concrete can be calculated as follows:

$$f'_{cc} = f'_{co} \left(-1.254 + 2.254 \sqrt{1 + \frac{7.94f'_l}{f'_{co}}} - 2 \frac{f'_l}{f'_{co}} \right) \quad (17)$$

where f'_{co} is the unconfined concrete compressive strength and f'_l is the effective lateral confining stress on the concrete. Therefore, ϕ can be calculated as follows:

$$\phi = -1.254 + 2.254 \sqrt{1 + \frac{7.94f'_l}{f'_{co}}} - 2 \frac{f'_l}{f'_{co}} \quad (18)$$

To simplify the calculation, it was specified in this paper that, approximately, $\phi = 1.65$.

According to the material properties and geometric dimensions of the connection of the specimen, the safe top-hinge depth for ensuring that the top longitudinal reinforcement remained in the elastic range was 102.75 mm, smaller than the value of $1/4d = 150$ mm proposed by Au (2010). Compared with the constant value of $1/4d$, the d_c obtained via Eq. (16) was influenced by various parameters. Therefore, the top-hinge depth calculated by Eq. (16) was more reasonable, accurate, and safe.

7 Conclusions

To realize a controllable bending moment in connections and the principle of “strong column weak beam”, a novel precast connection was proposed. Theoretical analysis of the connection, three low-cycle quasi-static loading tests, and numerical simulations were carried out in this paper. The conclusions were as follows:

- (1) The load-carrying mechanism of the novel precast connection was direct. The positive bending moment of the novel connection was governed by the yielding of the REDC core plate. The negative bending moment was governed by the yielding of the REDC core plate and the concrete compression zone at the bottom of the concrete top hinge. In addition, the positive and negative shear were transferred by the compression concrete zone and hidden corbel, respectively.
- (2) The seismic performance of the novel precast connection was excellent, particularly the energy-dissipation capacity and bearing capacity. The energy-dissipation capacity and bearing capacity were directly influenced by the REDC. When the thickness of the REDC core plate increased within a reasonable range, the energy dissipation capacity and bearing capacity of the novel precast connection could be improved.
- (3) The additional bending moment of the novel beam-to-column connection was significantly lower than that of the conventional connection, especially under a positive bending moment, which reduced the damage to the joint area and the column due to by the overstrength of the beam strength. In addition, the damage in the novel precast connection was mainly concentrated in the REDC. Therefore, the DAD approach could be realized in the novel beam-to-column connection. After an earthquake, these structures can be repaired quickly by replacing the REDCs.
- (4) Reducing the top-hinge depth (increasing the height of the vertical slot) reduced the additional bending moment and allowed the top longitudinal reinforcement to remain in the elastic range. This helped realize the “strong column weak beam” principle.

- (5) To reduce the additional bending moment under a negative bending moment, design suggestions and calculation formulas for the top-hinge depth were proposed. The additional bending moment of the novel precast connection designed by the proposed formulas could be reduced as much as possible. Therefore, the bending moment of the novel connection could be regarded as a controllable variable.

Acknowledgements The authors would like to acknowledge financial supports from the China National Key Research and Development Program (2019YFC1509305), the National Natural Science Foundation (51978165), and the Fundamental Research Funds for the Central Universities.

References

- ACI Committee 374 (2005) Acceptance criteria for moment frames based on structural testing and commentary. ACI Technical Document 374.1–05
- Amaris A, Pampanin S, Bull DK, Carr AJ (2008) Experimental investigation on a hybrid jointed precast frame with non-tearing floor connections. In: New Zealand society for earthquake engineering conference, New Zealand. <http://hdl.handle.net/10092/2659>
- Au EV (2010) The mechanics and design of a non-tearing floor connection using slotted reinforced concrete beams. Master Dissertation, University of Canterbury, Christchurch, New Zealand. <http://dx.doi.org/https://doi.org/10.26021/1323>
- Bacht T, Chase JG, MacRae G, Rodgers GW, Rabczuk T, Dhakal RP, Desombre J (2011) HF2V dissipator effects on the performance of a 3 story moment frame. *J Constr Steel Res* 67(12):1843–1849. <https://doi.org/10.1016/j.jcsr.2011.05.007>
- Blakeley RWG, Park R (1971) Seismic resistance of prestressed concrete beam-column assemblies. *ACI Struct J* 68(9):677–692
- Bull DK (2003) Understanding the complexities of designing diaphragms in buildings for earthquakes. In: symposium to celebrate the lifetime contributions of Tom Paulay and Bob Park, Christchurch, New Zealand. <https://doi.org/10.5459/bnzsee.37.2.70-88>
- Byrne JDR, Bull DK (2012) Design and testing of reinforced concrete frames incorporating the slotted beam detail. *Bull N Z Soc Earthq Eng* 45(2):77–83. <https://doi.org/10.5459/bnzsee.45.2.77-83>
- Chang B, Hutchinson T, Wang X, Englekirk R (2014) Seismic performance of beam-column subassemblies with high-strength steel reinforcement. *ACI Struct J* 111(6):1329
- Chang B, Hutchinson T, Wang X, Englekirk R (2013) Experimental seismic performance of beam-column subassemblies using ductile embeds. *J Struct Eng* 139(9):1555–1566. [https://doi.org/10.1061/\(ASCE\)ST.1943-541X.0000628](https://doi.org/10.1061/(ASCE)ST.1943-541X.0000628)
- Chi H, Liu J (2012) Seismic behavior of post-tensioned column base for steel self-centering moment resisting frame. *J Constr Steel Res* 78:117–130. <https://doi.org/10.1016/j.jcsr.2012.07.005>
- Englekirk RE (1995) Development and testing of a ductile connector for assembling precast concrete beams and columns. *PCI J* 40(2):36–51
- Englekirk RE (1996) An innovative design solution for precast prestressed concrete buildings in high seismic zones. *PCI J* 41(4):44–53
- Englekirk RE (2002) Design-construction of the paramount – a 39-story precast prestressed concrete apartment building. *PCI J* 47(4):56–71
- Fan L, Lu XL, Zhao B (2007) Summary of investigation on seismic behavior of precast concrete frame structures. *Struct Eng* 23(4):90–97 (in Chinese)
- Fenwick RC, Davidson BJ (1995) Elongation in ductile seismic-resistant reinforced concrete frames. Recent developments in lateral force Transfer in Buildings, ACI SP-157: 143–170.
- GB50011–2010 (2010) Code for seismic design of buildings (National Standards of the People's Republic of China). Ministry of Construction of the People's Republic of China. (in Chinese)
- GB50017–2017 (2017) Standard for design of steel structures (National Standards of the People's Republic of China). Ministry of Construction of the People's Republic of China. (in Chinese)
- Golondrino JCC, MacRae GA, Chase JG, Rodgers GW, Abu Akg, Clifton GC (2018) Asymmetrical friction connections post-heating behavior. *J Constr Steel Res* 149:119–129

- Golondrino JCC, MacRae GA, Chase JG, Rodgers GW, Clifton GC (2019) Asymmetric friction connection (AFC) design for seismic energy dissipation. *J Constr Steel Res* 157:70–81. <https://doi.org/10.1016/j.jcsr.2019.02.027>
- Huang X, Eatherton MR, Zhou Z (2020a) Initial stiffness of self-centering systems and application to self-centering-beam moment-frames. *Eng Struct* 203:109890. <https://doi.org/10.1016/j.engstruct.2019.109890>
- Hassoun MN, Al-Manaseer A (2020) *Structural concrete: theory and design*. John Wiley & sons
- Huang X, Zhou Z, Xie Q, Xue R, Zhu D (2017) Force distribution analysis of self-centering coupled-beams for moment-resisting-frames without floor elongation. *Eng Struct* 147: 328–344.
- Huang L, Zhou Z, Liu H, Si Y (2020b) Experimental investigation of hysteretic performance of self-centering glulam beam-to-column joint with friction dampers. *J Earthq Tsunami*. <https://doi.org/10.1142/S1793431121500056>
- Kenyon EM (2008) Predicting the seismic behavior of the Dywidag Ductile Connector (DDC) precast concrete system. Master Dissertation, California Polytechnic State University, San Luis Obispo, United States
- Köken A, Köroğlu MA (2013) Experimental study on beam-to-column connections of steel frame structures with steel slit dampers. *J Perform Constr Fac* 29(2):04014066
- Li C, Wu J, Zhang J, Tong C (2020) Experimental study on seismic performance of precast concrete frame with replaceable energy-dissipating connectors. *Eng Struct*. <https://doi.org/10.1016/j.engstruct.2020.111719>
- Liu H, Yan Q, Du X (2017) Seismic performance comparison between precast beam joints and cast-in-place beam joints. *Adv Struct Eng* 20(9):1299–1314. <https://doi.org/10.1177/1369433216674952>
- Mander JB, Cheng CT (1997) Seismic resistance of bridge piers based on damage avoidance design. Technical report NCEER-97-0014 State University of New York at Buffalo, Buffalo, USA: U.S. National center for earthquake engineering research (NCEER), Department of civil and environmental engineering
- Mander JB, Priestley MJ, Park R (1988) Theoretical stress-strain model for confined concrete. *J Struct Eng* 114(8):1804–1826. [https://doi.org/10.1061/\(ASCE\)0733-9445\(1988\)114:8\(1804\)](https://doi.org/10.1061/(ASCE)0733-9445(1988)114:8(1804))
- Mander TJ, Rodgers GW, Chase JG, Mander JB, MacRae GA, Dhakal RP (2009) Damage avoidance design steel beam-column moment connection using high-force-to-volume dissipators. *J Struct Eng* 135(11):1390–1397. [https://doi.org/10.1061/\(ASCE\)ST.1943-541X.0000065](https://doi.org/10.1061/(ASCE)ST.1943-541X.0000065)
- Marriott DJ (2009) The development of high-performance post-tensioned rocking systems for the seismic design of structures. Ph.D. Dissertation, University of Canterbury, Christchurch, New Zealand. <http://dx.doi.org/https://doi.org/10.26021/2391>
- Muir CA, Bull DK, Pampanin S (2013) Seismic testing of the slotted beam detail for reinforced concrete structures. Proceedings of the 2013 Structures Congress 2614–2625. <https://doi.org/10.1061/9780784412848.228>
- Muir CA (2014) Seismic performance of the slotted beam detail in reinforced concrete moment resisting frames. Ph.D. Dissertation, Department of Civil Engineering, University of Canterbury, New Zealand. <http://dx.doi.org/https://doi.org/10.26021/2268>
- Nakaki SD, Englekirk RE, Plaehn JL (1994) Ductile connectors for a precast concrete frame. *PCI J* 39(5):46–59
- Ohkubo M, Hamamoto T (2004) Developing reinforced concrete slotted beam structures to reduce earthquake damage and to enhance seismic structural performance. In: 13th world conference on earthquake engineering. Vancouver, B.C, Canada
- Ohkubo M, Matsuoka T, Yoshioka T, Anderson DL (2009) Shear transfer mechanism of reinforced concrete beams with a slot at the beam-end. *Proc Japan Concr Inst* 21(3):301–306
- Oh SH, Kim YJ, Ryu HS (2009) Seismic performance of steel structures with slit dampers. *Eng Struct* 31(9):1997–2008. <https://doi.org/10.1016/j.engstruct.2009.03.003>
- Oudah F, El-Hacha R (2017) Seismic performance of modified single-slotted beam concrete connection. *J Earthq Eng* 21(5):726–751. <https://doi.org/10.1080/13632469.2016.1206760>
- Peng B, Dhakal RP, Fenwick RC, Carr AJ (2009) Modelling of RC moment resisting frames with precast-prestressed flooring system. In: the 2009 New Zealand Society for Earthquake Engineering, Christchurch, New Zealand, April. <http://hdl.handle.net/10092/4302>
- Popovics S (1973) A numerical approach to the complete stress-strain curve of concrete. *Cem Concr Res* 3(5):583–599. [https://doi.org/10.1016/0008-8846\(73\)90096-3](https://doi.org/10.1016/0008-8846(73)90096-3)
- Priestley MJN, Macrae GA (1996) Seismic tests of precast beam-to-column joint subassemblages with unbonded tendons. *PCI J* 41(1):64–81
- Priestley MJN (1991) Overview of press research program. *PCI J* 4:50–57
- Priestley MJN (1996) The press program-current status and proposed plans for phase III. *PCI J* 2:22–40

- Rodgers GW (2009) Next generation structural technologies: implementing high force-to-volume energy absorbers. Ph.D. Dissertation, University of Canterbury, Christchurch, New Zealand. <http://dx.doi.org/https://doi.org/10.26021/1363>
- Rodgers GW, Solberg KM, Mander JB, Chase JG, Bradley BA, Dhakal RP (2012) High-force-to-volume seismic dissipators embedded in a jointed precast concrete frame. *J Struct Eng* 138(3):375–386. [https://doi.org/10.1061/\(ASCE\)ST.1943-541X.0000329](https://doi.org/10.1061/(ASCE)ST.1943-541X.0000329)
- Thomphon KJ (1975) Ductility of concrete frames under seismic loading. Ph.D. Dissertation, Department of Civil Engineering, University of Canterbury, New Zealand
- Tong C, Wu J, Hua K, Xie L (2020) Low-cycle fatigue life estimation curve for buckling-restrained braces based on cumulative plastic deformation. *J Earthq Eng.* <https://doi.org/10.1080/13632469.2020.1772152>
- Usami T, Wang C, Funayama J (2011) Low-cycle fatigue tests of a type of buckling-restrained braces. *Procedia Eng* 14:956–964. <https://doi.org/10.1016/j.proeng.2011.07.120>
- Vasconez RM, Naaman AE, Wight JK (1998) Behavior of HPFRC connections for precast concrete frames under reversed cyclic loading. *PCI J* 43(6):58–71
- Xie L (2020) Research on the mechanism of replaceable energy dissipation connector and its seismic performance in precast concrete frame joint. Ph.D. Dissertation, Southeast University (China), Nanjing, China. (in Chinese)

Publisher's Note Springer Nature remains neutral with regard to jurisdictional claims in published maps and institutional affiliations.